Materials Research Express

PAPER

MeV irradiation of tungsten nanowires: structural modifications

Joás Grossi[1,2,4], Jorge Kohanoff[3] and Eduardo M Bringa[1,4,5]

[1] CONICET, Argentina
[2] FCEN, Universidad Nacional de Cuyo, Mendoza, 5500, Argentina
[3] ASC, School of Mathematics and Physics, Queen's University Belfast, Belfast BT7 1NN, Northern Ireland, United Kingdom
[4] Facultad de Ingeniería, Universidad de Mendoza, Mendoza, 5500, Argentina
[5] Centro de Nanotecnología Aplicada, Facultad de Ciencias, Universidad Mayor, Chile

E-mail: joas.grossi@gmail.com

Keywords: nanowires, diffusion geometry, electronic stopping, hole, TTM-MD

OPEN ACCESS

RECEIVED
31 March 2020

REVISED
4 May 2020

ACCEPTED FOR PUBLICATION
12 May 2020

PUBLISHED
20 May 2020

Abstract

In this work we use the Two Temperature Model coupled to Molecular Dynamics (TTM-MD) to study swift heavy ion irradiation of W finite nanowires. Au projectiles are considered with energies ranging from 20 to 50 MeV, which correspond to electronic stopping values less than 20 keV nm^{-1} in the regime where electronic stopping is larger than nuclear stopping. Nanowires with diameters much smaller than the electron mean free path are considered for two different sizes with an aspect ratio ~3.7 between length and diameter. Nanowires display radiation-induced surface roughening, sputtering yields and the formation of point defects and di-vacancies. For the smallest size, a hole stays opened in the central part of the wire for $S_e > 12.6$ keV nm^{-1}. W nanofoams, considered as collections of connected nanowires like those simulated here, are expected to behave similarly under irradiation displaying radiation resistance for the electronic stopping range that has been considered. In fact, nanowires larger than tens of nm would be needed for defect accumulation and lack of radiation resistance.

1. Introduction

Significant work has been done on tungsten in the build up to ITER fusion reactor using a tungsten divertor and during the DEMO design phase in order to predict suitable operating temperature range and device lifetime [1, 2]. Useful progress has been made, but a full understanding of the effects of irradiation on tungsten has not yet been established. The primary concern for the effect of radiation damage on tungsten are changes in thermal conductivity and radiation embrittlement, but the effect of plasma-induced erosion is important as well because, it can seriously limit the lifetime of the wall components of the reactor and, in addition, the sputtered atoms can be transported into the core plasma where they lead to dilution of the fusion plasma and to energy losses. W nanofoams, called fuzz, form under fusion reactor conditions [2] and are expected to take heat loads that would crack bulk tungsten [3, 4]. In order to understand the behavior of nanoscale foams, they could be considered, within a coarse approximation, as collections of connected nanowires (NWs) [5], and thus study the behavior of individual irradiated NWs to infer the behavior of the whole nanostructure [5–9].

W NWs are not only involved in fuzzy surfaces that arise in fusion reactors but also in possible applications such as the pH measurement in ultra small cavities and other small systems of interest such as corrosion pits and biological cells [10]. W NWs of 100–300 nm in diameter show totally elastic bending, even after several load-unload cycles, this being unusual for a brittle material such as tungsten [11]. Moreover, W NWs of 10–50 nm in diameter are easy to manufacture by simple thermal treatment of W films. They show perfect straightness and neat appearance, being promising building blocks for nanoelectronics components [12].

The Two Temperature Model coupled to Molecular Dynamics (TTM-MD) is commonly used to represent the energy exchange between electrons and atoms in materials, usually under laser or swift heavy ion (SHI) irradiation. Electrons are considered as a fluid with certain thermal conductivity and heat capacity, which can couple and exchange energy with the nuclei via electron-phonon (e-ph) coupling. Since electrons are confined

due to finite size, an increase in surface scattering processes is expected. Hence, a larger e-ph coupling is expected as seen in recent experiments in metallic nanofoams [13] and thin films [14], but it is not clear how much compared to bulk. Also, studies [15, 16] show a dependence of the electron thermal conductivity with the diameter of the NW. It can drop by one order of magnitude compared to bulk values, as the diameter decreases and becomes of the order of the electron mean free path or smaller. In addition, in a previous work [17] we considered these two effects together in order to study irradiation in Au and W NWs. For W, due to the low electron thermal conductivity, there is localized heating from electrons to atoms at the track, with large temperature gradients. This singular feature leads to a combination of mechanisms such as sputtering, melt flow and vacancy formation which are very important in terms of structural modifications. This is not the case of Au.

Surface changes and defects have been observed for Ag [18, 19], Au [20], Cu [21], Ni and Co [22] nanowires underMeV irradiation. However, most of the experiments of irradiation of nanowires and nanofoams deal with the elastic regime [23, 24], without energy dissipation to electrons, being a few in the regime where electronic stopping is larger [25, 26].

Beets *et al* [27] presented a simulation/experimental integrated study examining crack propagation in nanoporous gold. They observed cracks in both samples propagating by the same mechanisms of sequential individual ligament failure. A series of nanowire computational deformation tests were conducted to understand individual ligament behavior, and how this influences the overall sample fracture. Nanowire samples were made in two different morphologies, cylindrical and hyperboloid. The observed failure conditions of the ligaments in the nanoporous gold digital sample are closer in value to the hyperboloid nanowires than to cylindrical wires. This finding is consistent with the fact that actual shape of the ligaments in the nanoporous gold sample is more similar to the hyperboloids than to the cylindrical wires. Hyperboloid nanowires could be considered as cylindrical wires connected to some wider junction of atoms. Here we use the TTM-MD model [17] to consider damage in W NWs after SHI irradiation thinking on the wires connected to some wider junction of atoms, giving the electrons the possibility to diffuse out of the wires according to the shape of the junction. Section 2 explains the methodology. Section 3 presents results on irradiation of NWs and discusses structural modifications observed. Finally, section 4 summarizes the results and extracts conclusions.

2. Method

The TTM-MD model [28, 29] pretends to describe the process by which a SHI traverses a material and leaves highly excited electrons in its path. For this purpose, a track with an elevated electronic temperature (T_e) is used to represent the energy lost by the ion with a given electronic stopping power (S_e). This energy diffuses and is transferred to the nuclei. Since the atomic motion is propagated via Molecular Dynamics (MD), the model has become a useful tool that has been extensively used for laser [30–32] and ion irradiation [28, 33, 34].

In a previous study [17], irradiation of Au and W finite nanowires was considered by using a TTM-MD approach that includes vacuum cells [35, 36], which are subcells of the electronic grid with $T_e = 0$. These act as effective boundary conditions in the finite difference scheme (FD), which makes the electronic energy diffuse only within the non-vacuum space. In most experiments, and even for nanofoams, one could consider that the NW is actually connected to some wider junction of atoms.

Here, we also consider an atomistic MD region with periodic boundary conditions in all directions, as shown in figure 1, but the outer electronic region which in [17] was a square-prism continuation of the nanowire, is replaced by a pyramidal shape, to account for the wider junction often observed in nanofoams [6]. Therefore, the electronic energy from the ion-track first diffuses along a grid in the square-prism shape overlapping the MD region, and finally is dispersed along a grid in the pyramidal shapes capping the MD region. The pyramids have a height h (along the nanowire axis z), and a base width b, along the x and y directions. Thermal baths keep the electronic temperature fixed at both ends of the grid along z. Heat transfer between the electronic and atomic subsystems uses an inhomogeneous Langevin thermostat [37].

Irradiation is assumed along a direction normal to the nanowire axis, and we consider ion tracks located at the centre of the NW, and along the x axis. This method can be applied to any nanowire orientation, but here we only consider nanowires with z axis along [001]. The electronic subcells used to model the track are approximately within a cylinder of 2.5 nm in diameter, which is an intermediate value according to a range of common values between 2 and 3 nm [38, 39], as shown in figure 1. The length of the track is the same as the diameter of the wire because the irradiation is taken perpendicular to it. The initial electronic temperature T_e in the track is calculated according to formula 1 in [17] for a given stopping power S_e.

Two scenarios are considered here: 20, 30, 40 and 50 MeV Au projectiles passing through a thin W nanowire (TNW) and a wide W nanowire (WNW). There are a few Au accelerators up to 50 MeV around the world, therefore it is experimentally possible to account for these scenarios. The electronic stopping values associated to the projectile energies are of 7.4, 10.7, 14.1 and 18.6 keV nm^{-1}, respectively. These stopping values are identified

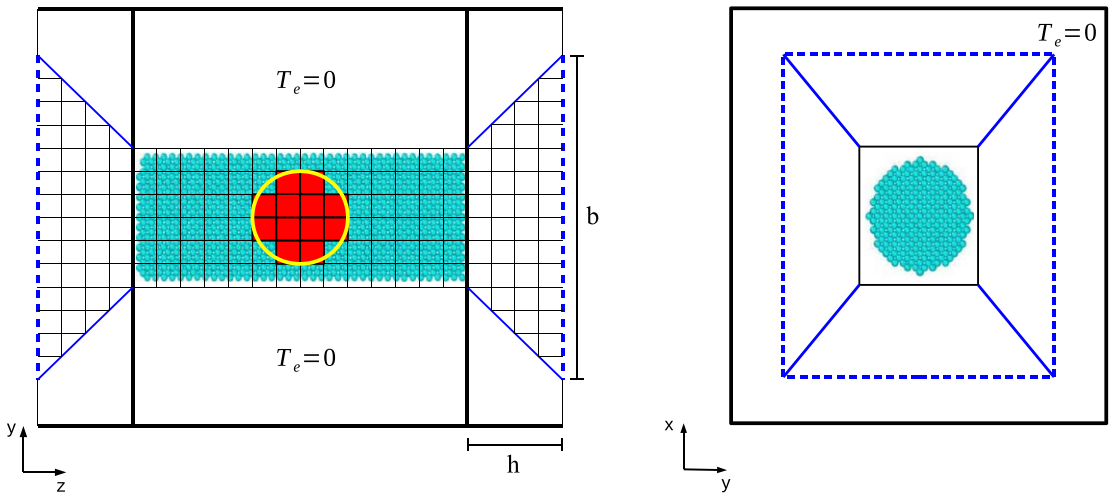

Figure 1. Schematic of the simulation (figures reprinted from [17]). The nanowire is inside the rectangle of thick black lines (MD box) and the overlying grid represents the cells of the electronic subsystem for the finite difference (FD) solution of T_e. Moreover, there is no energy transfer with the blank spaces (subcells for which $T_e = 0$). The electronic subcells used to model the irradiation-induced ion track are shown in red, they are approximately within a cylinder (yellow) of 2.5 nm in diameter. The axis of the nanowire is z while the ion track sits along the x axis, assuming normal incidence. For both the MD box and the electronic grid, periodic boundary conditions are represented by thick black lines. Energy transport is restricted to a square prism geometry surrounding the wire inside the MD box while it follows a square pyramid geometry outside the MD box as identified by the solid blue lines. On the right, the cross-section of the electronic grid is shown to better appreciate this combined geometry. h is the extension of the pyramid shape outside the MD box and b is the length of each side of the blue square. Boundary conditions with constant $T_e = 300$ K are considered in this work at the ends of the electronic grid (dashed blue lines).

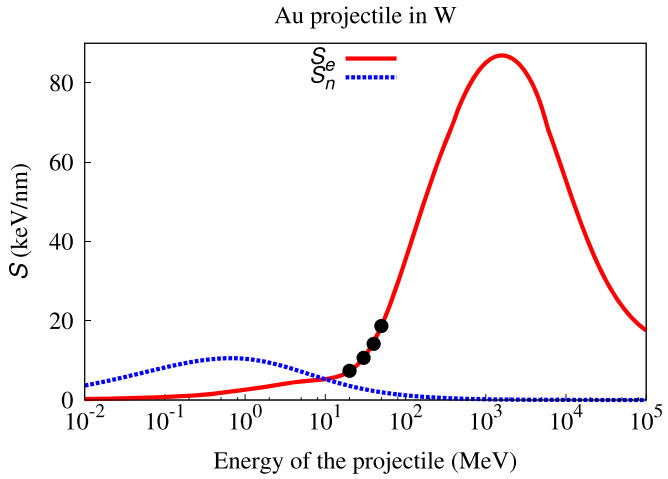

Figure 2. Electronic and nuclear stopping curves for a gold projectile in W according to SRIM [40]. Black circles correspond to 20, 30, 40 and 50 MeV Au projectile with $S_e = 7.4$, 10.7, 14.1 and 18.6 keV nm^{-1}, respectively.

by black circles in figure 2, where the electronic stopping curve is shown according to SRIM [40]. We are in the regime where electronic stopping is larger than nuclear stopping.

For nanowires considered as building units of a nanofoam, an aspect ratio between length and diameter in the range 1-3 is typically used [5, 7, 41]. Here we choose an aspect ratio ~3.7 being the TNW (~10000 atoms) of 3.7nm diameter and 14 nm length and the WNW (~80000 atoms) of 7.5 nm diameter and 28 nm length. These sizes are experimentally achievable nowadays [42, 43]. The embedded-atom-method (EAM) [44, 45] potential w eam4.fs [46] was used to describe the interaction among tungsten atoms. Wires were energetically minimized and thermalized to 300 K.

The electron thermal conductivity (K_e) is taken as in [17]. As the diameter of the nanowire decreases and becomes of the order of the electron mean free path or smaller, the electron thermal conductivity can drop by one order of magnitude compared to bulk values [15, 16]. The electron mean free path is of the order of 25 nm [47, 48] under the present conditions, much larger than the diameters of the NWs. Therefore, for NWs, the electron thermal conductivity was taken as $0.1K_e$, with K_e the bulk value. The e-ph coupling for W bulk [49] is

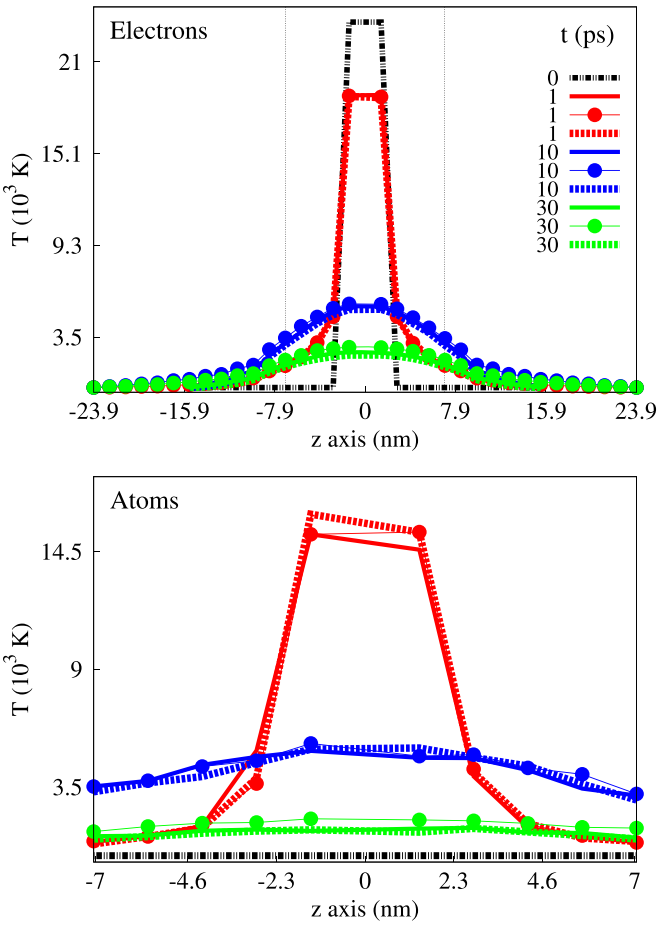

Figure 3. Average electronic and atomic temperature profiles for the TNW along the z axis at different times. $S_e = 10.7$ keV nm^{-1}. The parameters of the electronic grid (see figure 1) associated to the solid lines are h = 8.4 nm and b = 13.8 nm. Dashed lines: h and 1.85b, solid lines with circles: 2h and 1.85b.

1.65×10^{17}W m^{-3}K. For NWs, this value could be very different because of an increase of scattering-surface processes due to finite size, thus a larger e-ph coupling could be expected [13]. We take a value of 6 g as reference in this work, with g the associated bulk value, since the percentage of net energy transfer from electrons to atoms is similar to previous assumptions in MD simulations. Indeed, comparisons are made.

Each electronic grid cell has a volume of $2 \times 2 \times 1.4$ nm^3 with $9 \times 9 \times 22$ cells for TNW and $11 \times 11 \times 32$ for WNW. A MD time step of 0.01 fs has been used for all simulations which were conducted until the atomic temperature was well below the bulk melting temperature. Defect analysis and visualization were performed using the graphical package OVITO [50]. A version of the TTM-MD fix is available for download 'as is' [51].

Henceforth, the error bars displayed in some figures are related to the average over 4 independent simulations.

3. Results

In this work, we consider a pyramidal geometry for the extended electronic cell with baths keeping T_e fixed at the ends of the grid. By varying the parameters h and b associated to this shape, it is found that there are no significant changes in the atomic temperature profiles as seen in figure 3. Therefore, the physical situation remains the same regardless of particular choices of h and b. This is an important point because we see that the geometry associated to electron diffusion plays a key role when studying nanowires in a particular context. Of course, boundary conditions are important as well, but as far as we know, the diffusion geometry has not been taken into account in the literature. Figure 4 shows average electronic and atomic temperature profiles for W NWs for two geometries and different extensions of the electronic grid outside the MD box. For the junction shape used here, the atomic dynamics is not altered (as also shown in figure 3), but for the square prism geometry the effect is remarkable, the decay of the atomic temperature profiles is slower when doubling the extension h, hence the melting process continues for longer. This suggests that defects could be annihilated in a higher proportion allowing the structure to recover quickly and indeed, results would be significantly altered.

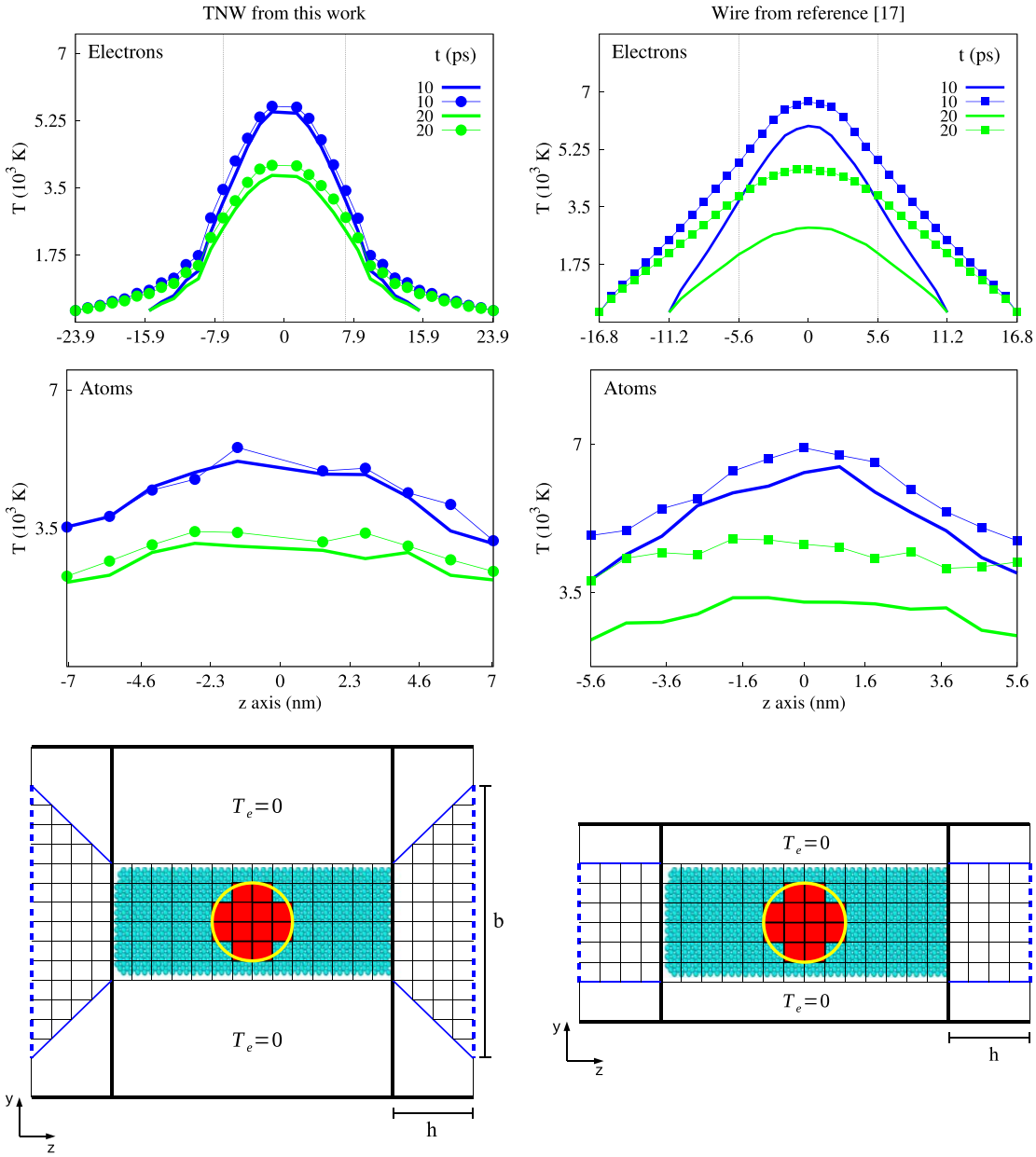

Figure 4. Average electronic and atomic temperature profiles for tungsten nanowires along the z axis at 10 and 20 ps. We have $S_e = 10.7$ keV nm^{-1}, $0.1K_e$ and $6g$ in all cases. Left: TNW from this work. Electronic grid parameters for solid lines are h = 8.4 nm and b = 13.8 nm, and for solid lines with circles are 2h and 1.85b. Right: tungsten nanowire of 3.9 nm diameter and 11.2 nm length from [17]. The electronic grid outside the MD cell has the same shape as the one surrounding the wire, that is, a square prism geometry, hence the extension h is the only parameter in this case. For solid lines h is 5.6nm and 2h for solid lines with squares. Also the schematics of the simulation geometries are shown below the curves accordingly. Figures on the right side have been reprinted and adapted from [17].

Therefore, diffusion geometry should be taken into account when studying nanowires which are part of a network.

In the remainder of this section, we describe results obtained for electronic parameters: (h = 8.4 nm, b = 13.8 nm) for TNW and (h = 8.4 nm, b = 18 nm) for WNW, so that the dispersion angle of the junction is the same for both wires.

According to spike models, the sputtering followed a quadratic relation for large electronic stoppings [52]. Using MD simulations with Lennard-Jones potentials, a linear relation was found between stopping and sputtering [39]. Also, with EAM [44, 45] potentials, Tucker *et al* found the same linear trend [53] for a gold target. For this behavior, Jakas *et al* proposed the following formula [54]

$$Y \approx C \times (R_{cyl}/U) \times (dE/dx)_{eff}, \quad (1)$$

being Y the sputtering yields, R_{cyl} the radius of the cylindrical region representing the ion-track, U the cohesive energy of the material, $(dE/dx)_{eff}$ the effective electronic stopping power and C a constant to be fitted. $(dE/dx)_{eff}$

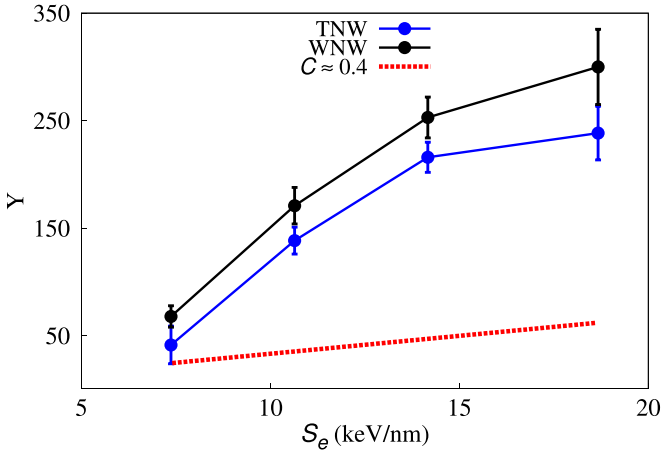

Figure 5. Sputtering yield Y for TNW and WNW for $S_e = 7.4, 10.7, 14.1$ and 18.6 keV nm^{-1}. Each circle results from the averaging over 4 values of the ejection yield with error bars showing the standard error of the mean. In addition, the curve for $C \approx 0.4$ represents twice the sputtering of a semi-infinite surface.

is the effective energy deposition on the atomic cores being this a fraction of the corresponding dE/dx, which is commonly assumed to be of 20% by MD simulations [53]. For a semi-infinite surface $C \approx 0.2$ using EAM and pair potentials [53, 54].

Figure 5 shows the sputtering yield for TNW and WNW for 20, 30, 40 and 50 MeV Au projectiles. These energies correspond to $S_e = 7.4, 10.7, 14.1$ and 18.6 keV nm^{-1}, respectively. There is no linear relation between the sputtering and the electronic stopping power, and the overlap between the error bars implies independence with respect to size. The energy that goes effectively from electrons to atoms corresponds to $(dE/dx)_{eff} \sim 30\%$ which is close to the assumption by MD simulations. It could be expected that twice of the sputtering corresponding to a semi-infinite surface ($C \approx 0.4$) could be a reference value to predict the two-side sputtering from the NW but, as seen in figure 5, the difference may be greater than a factor 5 as in the case for $S_e = 18.6$ keV nm^{-1}.

For the TNW, outer surfaces, defined by a meshing algorithm in the OVITO software [50], for $S_e = 10.7$, 12.6, 14.1, 16.5 and 18.6 keV nm^{-1} are shown in figure 6. There are in average 188 sputtered atoms when the hole opens at $S_e = 12.6$ keV nm^{-1}, if we consider the binding energy for tungsten (8 eV), then the energy that goes into sputtering corresponds to 10% of the energy that goes effectively to the track. This means that the rest of the energy goes into different channels such as heat diffusion, melt flow, defect formation, etc. In this work, the heat diffusion is anisotropic in the z axis and melt flow [17] accounts for this in figure 7, where atom displacements have a clear tendency towards the z axis, allowing the formation of a hole which has in average an elliptical form. An experimental work by Choi *et al* [55], shows that there is an anisotropic increase in electrical resistivity (along the axis of the wire) with decreasing cross-section in single crystal W nanowires. This increase could be up to 50% for nanowires of 15 nm width and could be even greater if there is roughness. This suggests that anisotropy for sufficiently small conductors results in anisotropic scattering processes that significantly affect electrical and mechanical properties. Regarding figure 6, it is also clear that the greater the stopping, the more noticeable is the local change in roughness around the track, partly due to the increasing size of the hole. In addition, for larger S_e, roughness changes along the wire are also observed even when they are slight.

For the WNW, there is no permanent hole for any stopping value. Surface cratering and sputtering appear in all cases and due to the size of the NW there is a clear local change in roughness around the ion track, as seen in figure 8, for a zoom of the outer surface close to that region. Also, roughening occurs due to sputtering and melt flow.

It is important to note that the hole opens in all cases considered in figure 6 for the TNW, but from $S_e \geqslant 12.6$ keV nm^{-1} onwards, the hole becomes permanent. In fact, there is available energy to form/open the hole from $S_e > 10$ keV nm^{-1} onwards but, in the range 10–12.5 keV nm^{-1}, it is not enough to keep the hole open until the cooling starts. We can summarize this point in this way: it is necessary that the hole stays open until the wire starts cooling down (recrystallization) so that the hole 'freezes' and remains open. For this wire, recrystallization begins at ≈13 ps and the energy imparted to electrons for $S_e = 12.6$ keV nm^{-1} (and consequently, the net energy transmitted to the cores) is the minimum necessary to have the hole open for 13 ps. On the other hand, we see no permanent hole for the WNW. For instance, the region around the ion-track starts cooling down at ≈70 ps. For this wide nanowire, the hole opens from $S_e \geqslant 14$ keV nm^{-1} onwards but there is not sufficient energy for the hole to remain open for 70 ps, not even for $S_e = 26$ keV nm^{-1} (which is a value

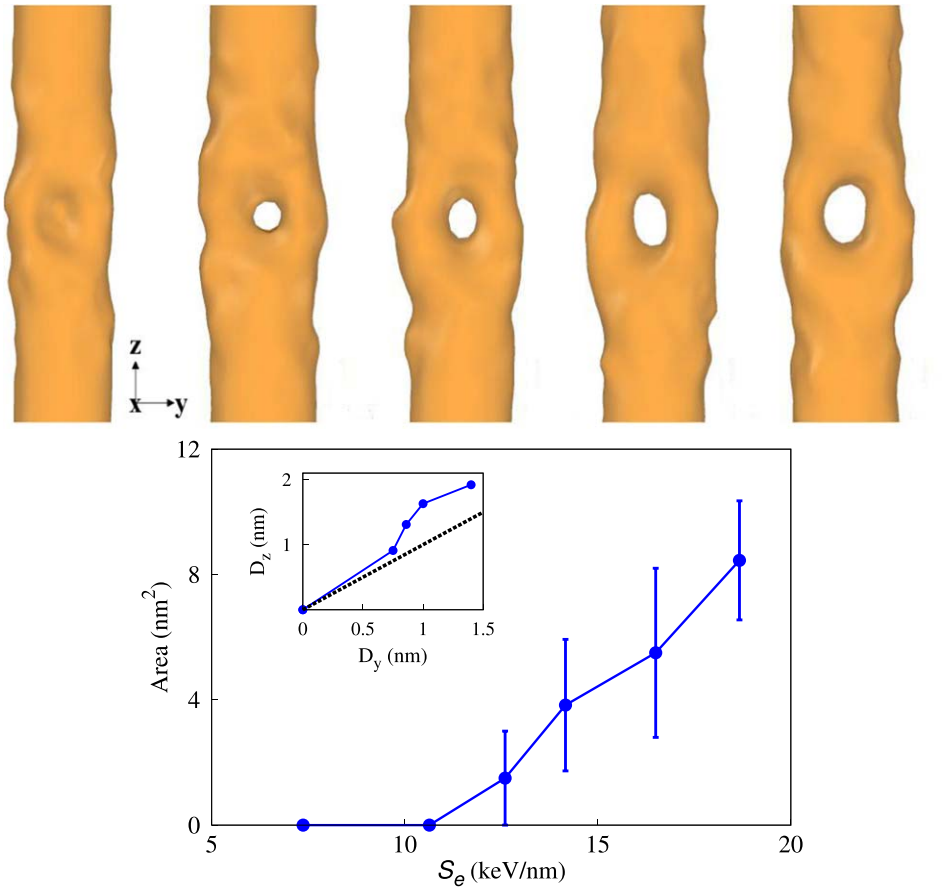

Figure 6. Outer surfaces of the TNW for $S_e = 10.7, 12.6, 14.1, 16.5$ and 18.6 keV nm^{-1} (from left to right). They were constructed by using the algorithm *Construct Surface Mesh* [56] implemented in OVITO [50]. The wire has already returned close to room temperature in all cases. The area of the hole is plotted with respect to each electronic stopping value. Each circle results from the averaging over 4 values of the hole's area with error bars showing the standard error of the mean. The hole adopts in average an elliptical shape and to account for this, average values of diameters in z and y axis are plotted for each S_e. In addition, the spherical trend is displayed with a dashed line.

outside of the experimental range considered here), where the hole stays open for ~30 ps. Finally, we can summarize the idea of this paragraph as follows: permanent holes could be seen for thin wires due to the hole development is fast and cooling starts very early, and of course, this can be tested experimentally due to the stopping range considered here.

Point defects and di-vacancies are formed in both nanowires and eventually a few tri-vacancies in the case of the WNW. For the TNW, defects are found along the wire while they remain around the track region for the WNW. Although defect distribution is different in the wires, the number of vacancies per atom is similar, as identified in figure 8. To visualize vacancies, the Voronoi tessellation implemented in OVITO [50] was considered, which allows to identify missing atoms when the Voronoi volumes of certain atoms are above a reference value (which is the typical volume value for atoms having a certain crystal structure).

For bulk tungsten, the number of defects is expected to follow a linear trend [29] with S_e, but for nanowires the behaviour is quite different as identified from the curves in figure 8. Starting with the TNW (blue line), there is an increase in the number of vacancies from 7.4 to 10.7 keV nm^{-1}, then it decreases until the hole keeps open and increases again. What we see from simulations is that certain processes acquire more or less importance depending on the stopping range considered. From 7.4 to 10.7 keV nm^{-1}, the energy is mainly destined for defect formation and not for the hole development. In the next stage, there is a decay in the number of vacancies because the hole starts opening, the longer the hole is kept open, the less energy that goes into defect formation. When the hole becomes permanent, then there is sufficient energy not only to increase the size of the permanent hole, but also to form vacancies, hence the number of them rises again. For the WNW (black line), we see a growth in the number of vacancies followed by a decay, but for this larger size there is no permanent hole.

Diffusivities for single vacancies and di-vacancies are 80.7 and 0.1347 nm^2 s^{-1}, respectively [57, 58]. Then, defects are expected to disappear within seconds for both nanowires while it may be possible to observe the changes in roughness of the wires during experimental times.

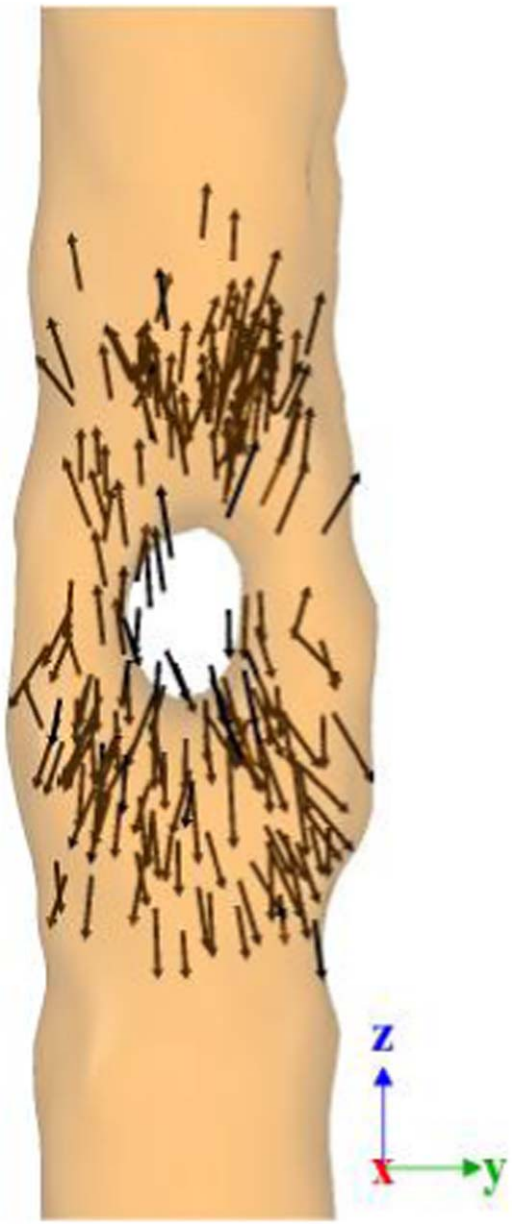

Figure 7. Outer surface of the TNW for $S_e = 18.6$ keV nm^{-1}. The algorithm *Displacements Vectors* implemented in OVITO [50] was used to determine how much the atoms have displaced with respect to their initial positions at the beginning of the simulation. Displacement vectors corresponding to atoms that have displaced 2nm or more in z direction are displayed. The arrows are scaled by 0.3 to better appreciate the anisotropy in the z direction.

There is no formation of dislocations in any of the wires for the electronic stopping range considered in this work. Figure 9 shows pressure (P_{zz}) and shear stress (σ_{shear}) curves for the WNW for the highest stopping value. The shear stress was calculated as $\sigma_{shear} = 1/2[\sigma_{zz} - (\sigma_{xx} + \sigma_{yy})/2]$. A pressure peak ~16.5 GPa is reached within half a picosecond, which decays rapidly in time. For shear, the maximum peak ~5.5 GPa is reached within one picosecond and its decay is fast as in the pressure case. Homogeneous nucleation of plasticity in bulk W requires pressures over 30 GPa for shocks along [001], [011] or [111] [59]. Also, for W nanowires under tension, the elastic limit is greater than 25 GPa, for nanowires with square cross-section close to 2.5 nm $\times$ 2.5 nm, and orientations along [001], [011] or [111] [60]. Our stress values are significantly smaller than those values, and they are only reached within a small region during very short times. Therefore, the track-induced stresses are not enough to drive heterogeneous dislocation nor twin nucleation from the surfaces of the nanowires studied here.

All simulations for both nanowires, considering the range of electronic stopping values, show sputtering, surface cratering, point defects and di-vacancies. The development of the hole is seen in both wires, but it only remains open for the TNW (for $S_e > 12.6$ keV nm^{-1}). For both wires, local changes in roughness are observed but due to size, the local effects stand out better for the WNW.

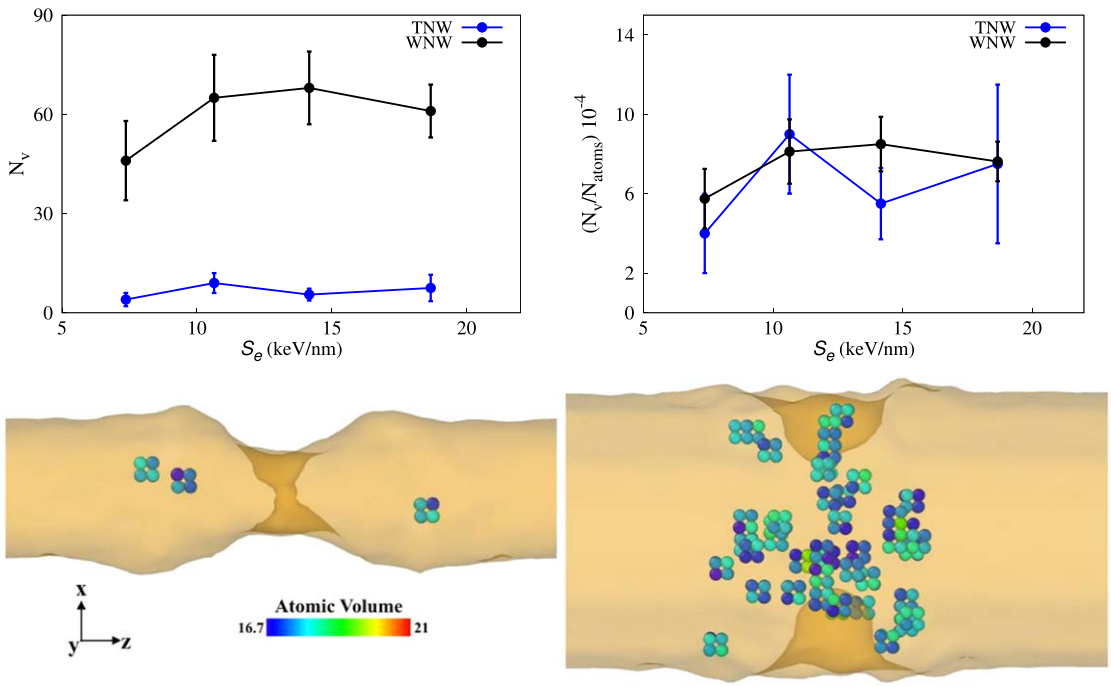

Figure 8. Up: number of vacancies N_v (counted as single vacancies) for TNW and WNW for $S_e = 7.4, 10.7, 14.1$ and 18.6 keV nm^{-1}. The same on the right, but for the number of vacancies normalized by the total number of atoms of the wire (N_{atoms}). Each circle results from the averaging over 4 simulations with error bars showing the standard error of the mean. Bottom: outer surfaces for TNW (left) and WNW (right) for $S_e = 14.1$ keV nm^{-1}, constructed by the algorithm *Construct Surface Mesh* [56] implemented in OVITO [50]. Vacancies are dispersed along the thin nanowire while they are located around the ion-track for the wide nanowire. Each vacancy is represented by a cube of 8 atoms: tungsten atoms, which have a body-centered cubic crystal structure, have an atomic volume of 15.6 Å^3 by doing the Voronoi tessellation implemented in OVITO [50]. Therefore, if the atom of the center is missing (vacancy) then the 8 surrounding atoms have larger Voronoi volumes, as identified in the corresponding legend.

4. Summary and future outlooks

NWs with an aspect ratio between length and diameter of 3.7 are studied here. One of 3.7 nm diameter and 14 nm length, and another wire of 7.5 nm diameter and 28 nm length. A cylindrical track perpendicular to the axis of the wire was considered to model irradiation. The elevated electronic temperatures in the track correspond to S_e below 20 keV nm^{-1}. For tungsten, where there is localized heating at the track, with large temperature gradients, single vacancies and di-vacancies are observed for the stopping power range considered here. According to the associated diffusivity values [57, 58], these defects are expected to migrate to the surface and disappear, this would imply that nanowires are in fact radiation resistant in agreement with the radiation resistance present in nanofoams underkeV irradiation [61]. However, the large temperature gradients lead to a rapid ejection of atoms from the track, leading to changes in the topology of the wires. This produces significant roughening for smaller nanowires, including the possibility of a permanent hole, in addition to roughening produced by melt flow. The hole could be useful to infiltrate genes in plant cells [62] to allow DNA integration into the host genome. For larger nanowires, no permanent hole is observed but there is significant roughening around the track region. Metallic nanowires have excellent electrical and thermal conductivity, but the size can dramatically affect these two properties. Recently, Tamm *et al* [63, 64] have implemented a new version of the TTM-MD model in which they replace the scalar values of friction and random forces over individual particles with many-body forces that act in a correlated manner over different particles. This generalization allows modeling the electronic subsystem in a metal as a generalized Langevin bath equipped with a concept of locality due to correlation. First-principles time-dependent density functional theory is used to provide electronic stopping and electron phonon interactions and to feed the model. Although the computational cost of this model is about 50% higher than the standard TTM-MD (1.5 times slower), it would be interesting to see how the correlation between particles would affect the results shown in this work. Therefore, characterization of wires should be a very important part of metallic NWs research in order to understand how to use them in advanced building applications [65].

To account for a scenario in which a NW is connected to a wider junction of atoms, the electronic grid was extended beyond the MD box with a pyramidal shape. The geometry associated to electron diffusion must be taken into account when studying nanowires in a particular context due to the possible implications that it could

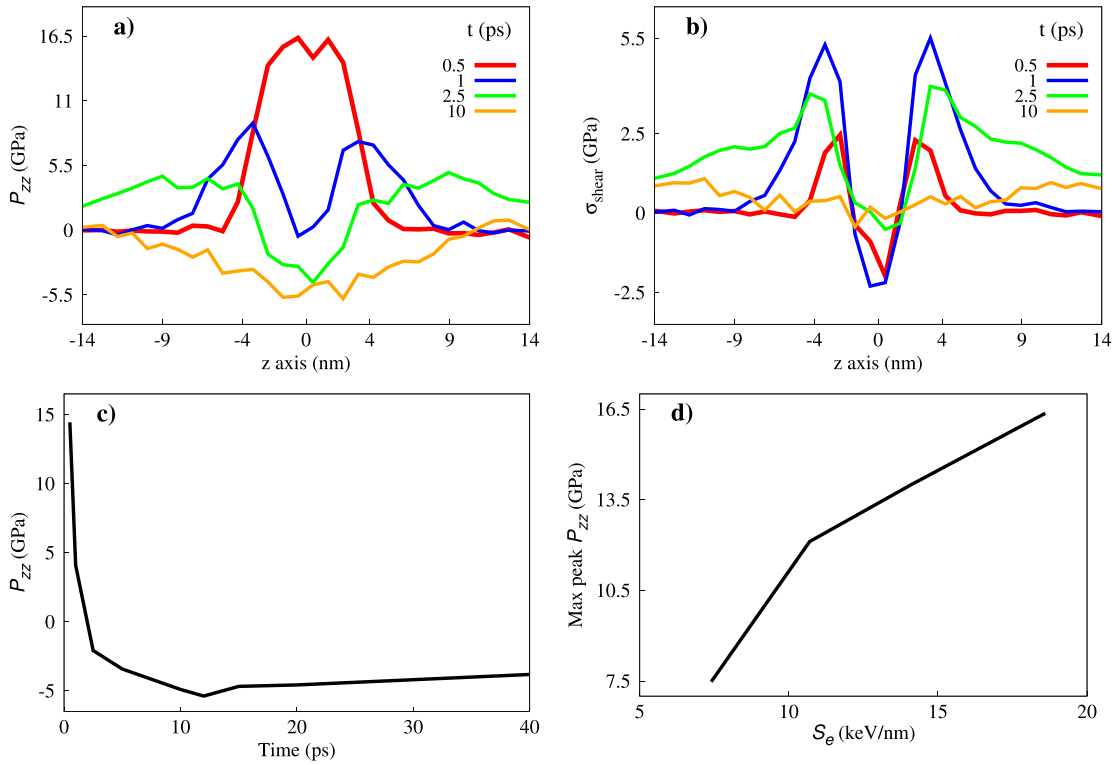

Figure 9. (a) and (b) P_{zz} and σ_{shear} in z axis for the WNW for $S_e = 18.6$ keV nm^{-1} at different times. Curves were obtained by using the algorithm *Bin and Reduce* implemented in OVITO [50]. Bins are defined by cutting the MD simulation box in a certain direction. In our case, we cut in the z direction considering 28 bins of 22.34 nm × 22.34 nm × 1 nm each. We sum P_{zz} (or σ_{shear}) for all the atoms inside a bin and divide this value by the bin volume by using the command *sum divided by bin volume*, which is part of the algorithm. In addition, we divide the latter by the solid volume fraction (given by the algorithm *Construct Surface Mesh* [56]), which represents the solid volume of the wire with respect to the simulation box, to account for pressure (or shear) with respect to the wire. The solid volume fraction changes 6% during the simulation due to the expansion of the material. The largest expansion occurs in the region of the ion-track due to the hole development and its subsequent healing. Therefore, we take a cylindrical section of the wire of 6.8nm in length, in the middle of it containing the track in order to see how the solid volume fraction changes in this zone and how P_{zz} is modified. In fact, according to (c), the maximum P_{zz} is 14.4 GPa which is less than 16.3 GPa in (a). In this middle section of the wire the solid volume fraction changes 10%. (d) Curve of maximum peaks of P_{zz} for $S_e = 7.4$, 10.7, 14.1 and 18.6 keV nm^{-1}.

have on atomic dynamics, hence on defect formation and structural modifications. Baths kept T_e fixed at the ends of the electronic grid. Nanofoams, considered as collections of connected NWs like those simulated here, are expected to behave similarly under irradiation displaying radiation resistance for $S_e < 20$ keV nm^{-1}, at low-moderate dose [5]. Thicker NW cause defect accumulation around the ion track and high dose could also cause defect accumulation as discussed for keV irradiation [5, 66]. Therefore, we estimate that NWs larger than tens of nm would be needed for defect accumulation and lack of radiation resistance.

Acknowledgments

JG, EMB, and JK thank EC-H2020-MSC-RISE-2014, Project number 643 998 ENACT. EMB thanks funding from a SIIP-UNCuyo grant. He also thanks fruitful discussion with A Correa and A Tamm JG greatly appreciative to T Todorov at Queen's University Belfast and to E Artacho at the University of Cambridge for helpful discussions on electronic stopping power and electron thermal conductivity in nanowires. This work used the Toko Cluster from FCEN-UNCuyo, which is part of the SNCAD-MinCyT, Argentina.

ORCID iDs

Joás Grossi https://orcid.org/0000-0001-7854-0312
Jorge Kohanoff https://orcid.org/0000-0002-8237-7543
Eduardo M Bringa https://orcid.org/0000-0002-1403-1954

References

[1] Rieth M *et al* 2013 Recent progress in research on tungsten materials for nuclear fusion applications in Europe *J. Nucl. Mater.* **432** 482–500
[2] Ueda Y, Coenen J, De Temmerman G, Doerner R, Linke J, Philipps V and Tsitrone E 2014 Research status and issues of tungsten plasma facing materials for ITER and beyond *Fusion Eng. Des.* **89** 901–6
[3] Wright G, Brunner D, Baldwin M, Doerner R, Labombard B, Lipschultz B, Terry J and Whyte D 2012 Tungsten nano-tendril growth in the Alcator C-Mod divertor *Nucl. Fusion* **52** 042003
[4] Huber A *et al* 2014 Investigation of the impact of transient heat loads applied by laser irradiation on ITER-grade tungsten *Phys. Scripta* **2014** 014005
[5] Bringa E *et al* 2012 Are nanoporous materials radiation resistant? *Nano Lett.* **12** 3351–5
[6] Fu E, Caro M, Zepeda-Ruiz L, Wang Y, Baldwin K, Bringa E, Nastasi M and Caro A 2012 Surface effects on the radiation response of nanoporous Au foams *Appl. Phys. Lett.* **101** 191607
[7] Figueroa E, Tramontina D, Gutiérrez G and Bringa E 2015 Mechanical properties of irradiated nanowires -A molecular dynamics study *J. Nucl. Mater.* **467** 677–82
[8] Liu W, Chen P, Qiu R, Khan M, Liu J, Hou M and Duan J 2017 A molecular dynamics simulation study of irradiation induced defects in gold nanowire *Nucl. Instrum. Meth.* B **405** 22–30
[9] Zhang C, Li Y, Zhou W, Hu L and Zeng Z 2015 Anti-radiation mechanisms in nanoporous gold studied via molecular dynamics simulations *J. Nucl. Mater.* **466** 328–33
[10] Fenster C, Smith A, Abts A, Milenkovic S and Hassel A 2008 Single tungsten nanowires as pH sensitive electrodes *Electrochem. Commun.* **10** 1125–8
[11] Cimalla V *et al* 2008 Nanomechanics of single crystalline tungsten nanowires *J. Nanomater.* **2008** 44
[12] Lee Y H, Choi C H, Jang Y T, Kim E K, Ju B K, Min N K and Ahn J H 2002 Tungsten nanowires and their field electron emission properties *Appl. Phys. Lett.* **81** 745–7
[13] Zheng Q *et al* 2018 Dynamics of electron-phonon coupling in bicontinuous nanoporous gold *J. Phys. Chem.* C **122** 16368–73
[14] Singh U, Pannu C, Agarwal D, Ojha S, Khan S, Ghosh S and Avasthi D 2017 Large electronic sputtering yield of nanodimensional Au thin films: dominant role of thermal conductivity and electron phonon coupling factor *J. Appl. Phys.* **121** 095308
[15] Stewart D and Norris P 2000 Size effects on the thermal conductivity of thin metallic wires: microscale implications *Microscale Therm. Eng.* **4** 89–101
[16] Hopkins P, Norris P, Phinney L, Policastro S and Kelly R 2008 Thermal conductivity in nanoporous gold films during electron-phonon nonequilibrium *J. Nanomater.* **2008** 22
[17] Grossi J, Kohanoff J, Todorov T, Artacho E and Bringa E 2019 Electronic heat transport versus atomic heating in irradiated short metallic nanowires *Phys. Rev.* B **100** 155434
[18] Shang Z, Li J, Fan C, Chen Y, Li Q, Wang H, Shen T and Zhang X 2018 *In situ* study on surface roughening in radiation-resistant Ag nanowires *Nanotechnology* **29** 215708
[19] Shehla H, Ishaq A, Khan Y, Javed I, Saira R, Shahzad N and Maaza M 2016 Ion beam irradiation-induced nano-welding of Ag nanowires *Micro Nano Lett.* **11** 34–7
[20] Cheng Y *et al* 2017 Surface modification and damage of MeV-energy heavy ion irradiation on gold nanowires *Nanomaterials* **7** 108
[21] Gupta R, Chauhan R, Chakarvarti S and Kumar R 2019 Effect of SHI on properties of template synthesized Cu nanowires *Ionics* **25** 341–352
[22] Park S, Hong Y, Lee Y, Bae S and Joo J 2009 Surface modification of Ni and Co metal nanowires through MeV high energy ion irradiation *Curr. Appl. Phys.* **9** 847–51
[23] Bedin S, Makhin'ko F, Ovchinnikov V, Gerasimenko N and Zagorskiy D 2017 Radiation stability of metal nanowires *IOP Conf. Ser. Mater. Sci. Eng.* **168** 012096
[24] Sofiah A, Samykano M, Kadirgama K, Mohan R and Lah N 2018 Metallic nanowires: mechanical properties-theory and experiment *Appl. Mater. Today* **11** 320–37
[25] Wang J, Hu Z, Li R, Liu X, Xu C, Wang H, Wu Y, Fu E and Lu Z 2018 Influences of Au ion radiation on microstructure and surface-enhanced Raman scattering of nanoporous copper *Nanotechnology* **29** 184001
[26] Gupta R and Kumar R 2019 Electronic energy loss (S_e) sensitivity of electrochemically synthesized free-standing Cu nanowires irradiated by 120 MeV high energy ion beam of different atomic mass *Appl. Phys.* A **125** 835
[27] Beets N, Stuckner J, Murayama M and Farkas D 2020 Fracture in nanoporous gold: an integrated computational and experimental study *Acta Mater.* **185** 257–70
[28] Duffy D, Itoh N, Rutherford A and Stoneham A 2008 Making tracks in metals *J. Phys.: Condens. Matter* **20** 082201
[29] Khara G, Murphy S and Duffy D 2017 Dislocation loop formation by swift heavy ion irradiation of metals *J. Phys.: Condens. Matter* **29** 285303
[30] Schäfer C, Urbassek H and Zhigilei L 2002 Metal ablation by picosecond laser pulses: a hybrid simulation *Phys. Rev.* B **66** 115404
[31] Ivanov D and Zhigilei L 2003 Combined atomistic-continuum modeling of short-pulse laser melting and disintegration of metal films *Phys. Rev.* B **68** 064114
[32] Rosandi Y, Grossi J, Bringa E and Urbassek H 2018 The laser ablation of a metal foam: the role of electron-phonon coupling and electronic heat diffusivity *J. Appl. Phys.* **123** 034305
[33] Duffy D and Rutherford A 2006 Including the effects of electronic stopping and electron-ion interactions in radiation damage simulations *J. Phys.: Condens. Matter* **19** 016207
[34] Rutherford A and Duffy D 2007 The effect of electron-ion interactions on radiation damage simulations *J. Phys.: Condens. Matter* **19** 496201
[35] Norman G, Starikov S, Stegailov V, Saitov I and Zhilyaev P 2013 Atomistic modeling of warm dense matter in the two-temperature state *Contrib. Plasm. Phys.* **53** 129–39
[36] Pisarev V and Starikov S 2014 Atomistic simulation of ion track formation in UO_2 *J. Phys.: Condens. Matter* **26** 475401
[37] Phillips C and Crozier P 2009 An energy-conserving two-temperature model of radiation damage in single-component and binary Lennard-Jones crystals *J. Chem. Phys.* **131** 074701
[38] Johnson R and Schou J 1993 Sputtering of inorganic insulators *Mat. Fys. Medd. K. Dan. Vidensk. Selsk.* **43** 403-493
[39] Bringa E, Johnson R and Jakas M 1999 Molecular-dynamics simulations of electronic sputtering *Phys. Rev.* B **60** 15107
[40] Ziegler J, Ziegler M and Biersack J 2010 SRIM-The stopping and range of ions in matter (2010) *Nucl. Instrum. Meth.* B **268** 1818–23

[41] Caro M, Mook W, Fu E, Wang Y, Sheehan C, Martinez E, Baldwin J and Caro A 2014 Radiation induced effects on mechanical properties of nanoporous gold foams *Appl. Phys. Lett.* **104** 233109
[42] García M, Batalla P and Escarpa A 2014 Metallic and polymeric nanowires for electrochemical sensing and biosensing *Trac-Trend Anal. Chem.* **57** 6–22
[43] Wang S, Shan Z and Huang H 2017 The mechanical properties of nanowires *Adv. Sci.* **4** 1600332
[44] Daw M and Baskes M 1984 Embedded-atom method: Derivation and application to impurities, surfaces, and other defects in metals *Phys. Rev.* B **29** 6443
[45] Finnis M and Sinclair J 1984 A simple empirical N-body potential for transition metals *Philos. Mag.* A **50** 45–55
[46] Marinica M, Ventelon L, Gilbert M, Proville L, Dudarev S, Marian J, Bencteux G and Willaime F 2013 Interatomic potentials for modelling radiation defects and dislocations in tungsten *J. Phys.: Condens. Matter* **25** 395502
[47] Gall D 2016 Electron mean free path in elemental metals *J. Appl. Phys.* **119** 085101
[48] Lüth H 1995 *Surfaces and Interfaces of Solid Materials* (New York: Springer-Verlag Berlin Heidelberg)
[49] Lin Z, Zhigilei L and Celli V 2008 Electron-phonon coupling and electron heat capacity of metals under conditions of strong electron-phonon nonequilibrium *Phys. Rev.* B **77** 075133
[50] Stukowski A 2009 Visualization and analysis of atomistic simulation data with OVITO-the open visualization tool *Model. Simul. Mater. Sc.* **18** 015012
[51] A version of the TTM-MD fix is available for download is here https://sites.google.com/site/simafweb/software/fix_ttm2.tar.gz
[52] Sigmund P and Szymonski M 1984 Temperature-dependent sputtering of metals and insulators *Appl. Phys.* A **33** 141–52
[53] Tucker O, Ivanov D, Zhigilei L, Johnson R and Bringa E 2005 Molecular dynamics simulation of sputtering from a cylindrical track: EAM versus pair potentials *Nucl. Instrum. Meth.* B **228** 163–9
[54] Jakas M, Bringa E and Johnson R 2002 Fluid dynamics calculation of sputtering from a cylindrical thermal spike *Phys. Rev.* B **65** 165425
[55] Choi D, Moneck M, Liu X, Oh S, Kagan C, Coffey K and Barmak K 2013 Crystallographic anisotropy of the resistivity size effect in single crystal tungsten nanowires *Sci. Rep.* **3** 2591
[56] Stukowski A 2014 Computational analysis methods in atomistic modeling of crystals *JOM* **66** 399–407
[57] Becquart C, Domain C, Sarkar U, Debacker A and Hou M 2010 Microstructural evolution of irradiated tungsten: *Ab initio* parameterisation of an OKMC model *J. Nucl. Mater.* **403** 75–88
[58] Martin-Bragado I, Rivera A, Valles G, Gomez-Selles J and Caturla M 2013 MMonCa: an Object Kinetic Monte Carlo simulator for damage irradiation evolution and defect diffusion *Comput. Phys. Commun.* **184** 2703–10
[59] Liu C, Xu C, Cheng Y, Chen X and Cai L 2015 Orientation-dependent responses of tungsten single crystal under shock compression via molecular dynamics simulations *Comput. Mater. Sci.* **110** 359–67
[60] Bin M, Rao Q H and He Y H 2014 Effect of crystal orientation on tensile mechanical properties of single-crystal tungsten nanowire *T. Nonferr. Metal Soc.* **24** 2904–10
[61] Zhang X *et al* 2018 Radiation damage in nanostructured materials *Prog. Mater. Sci.* **96** 217-321
[62] Demirer G, Zhang H, Matos J, Chang R, Chio L, Staskawicz B and Landry M 2018 Nanoparticle-guided biomolecule delivery for transgene expression and gene silencing in mature plants *BioRxiv* **114** 179549
[63] Tamm A, Caro M, Caro A, Samolyuk G, Klintenberg M and Correa A 2018 Langevin dynamics with spatial correlations as a model for electron-phonon coupling *Phys. Rev. Lett.* **120** 185501
[64] Tamm A, Caro M, Caro A and Correa A 2019 Role of electrons in collision cascades in solids. II. Molecular dynamics *Phys. Rev.* B **99** 174302
[65] Shah K and Xiong T 2019 Multifunctional metallic nanowires in advanced building applications *Materials* **12** 1731
[66] Ruestes C, Anders C, Bringa E and Urbassek H 2018 Nanoindentation tests of heavy-ion-irradiated Au foams-molecular dynamics simulation *J. Appl. Phys.* **123** 225903